Cornea microstructure and mechanical responses measured with nonlinear optical and optical coherence microscopy using sub-10-fs pulses

Qiaofeng Wu, Brian E. Applegate, and Alvin T. Yeh

Department of Biomedical Engineering, Texas A&M University, 337 Zachry Engineering Center, 3120 TAMU, College Station, TX 77843, USA

ayeh@tamu.edu

Abstract: A combined nonlinear optical microscopy (NLOM) and optical coherence microscopy (OCM) imaging system has been assembled in order to simultaneously capture co-registered volumetric images of corneal morphology and biochemistry. Tracking of cell nuclei visible in the OCM volume enabled the calculation of strain depth profile in response to changes in intraocular pressure for rabbit cornea stroma. Results revealed nonlinear responses with a depth dependent strain distribution, exhibiting smaller strains in the anterior and larger strains in the posterior stroma. Cross-sectional images of collagen lamellae, visible in NLOM, showed inhomogeneous collagen structure along the anterior-posterior direction that correlated well with the noted heterogeneous corneal mechanical responses.

©2011 Optical Society of America

OCIS codes: (180.1790) Confocal microscopy; (170.4500) Optical coherence tomography; (170.5810) Laser scanning microscopy; (190.4180) Multiphoton processes; (170.6935) Tissue characterization

References and links

1. C. Kirwan and M. O'Keefe, "Measurement of intraocular pressure in LASIK and LASEK patients using the Reichert Ocular Response Analyzer and Goldmann applanation tonometry," J. Refract. Surg. **24**(4), 366–370 (2008).
2. M. Kohlhaas, E. Spoerl, A. G. Boehm, and K. Pollack, "A correction formula for the real intraocular pressure after LASIK for the correction of myopic astigmatism," J. Refract. Surg. **22**(3), 263–267 (2006).
3. J. Liu and C. J. Roberts, "Influence of corneal biomechanical properties on intraocular pressure measurement: quantitative analysis," J. Cataract Refract. Surg. **31**(1), 146–155 (2005).
4. J. S. Pepose, S. K. Feigenbaum, M. A. Qazi, J. P. Sanderson, and C. J. Roberts, "Changes in corneal biomechanics and intraocular pressure following LASIK using static, dynamic, and noncontact tonometry," Am. J. Ophthalmol. **143**(1), 39–47.e1 (2007).
5. C. Roberts, "The cornea is not a piece of plastic," J. Refract. Surg. **16**(4), 407–413 (2000).
6. J. O. Hjortdal, "Regional elastic performance of the human cornea," J. Biomech. **29**(7), 931–942 (1996).
7. B. Jue and D. M. Maurice, "The mechanical properties of the rabbit and human cornea," J. Biomech. **19**(10), 847–853 (1986).
8. T. J. Shin, R. P. Vito, L. W. Johnson, and B. E. McCarey, "The distribution of strain in the human cornea," J. Biomech. **30**(5), 497–503 (1997).
9. H. Aghamohammadzadeh, R. H. Newton, and K. M. Meek, "X-ray scattering used to map the preferred collagen orientation in the human cornea and limbus," Structure **12**(2), 249–256 (2004).
10. M. Abahussin, S. Hayes, N. E. Knox Cartwright, C. S. Kamma-Lorger, Y. Khan, J. Marshall, and K. M. Meek, "3D collagen orientation study of the human cornea using X-ray diffraction and femtosecond laser technology," Invest. Ophthalmol. Vis. Sci. **50**(11), 5159–5164 (2009).
11. Q. Wu and A. T. Yeh, "Rabbit cornea microstructure response to changes in intraocular pressure visualized by using nonlinear optical microscopy," Cornea **27**(2), 202–208 (2008).
12. L. J. Müller, E. Pels, and G. F. J. M. Vrensen, "The specific architecture of the anterior stroma accounts for maintenance of corneal curvature," Br. J. Ophthalmol. **85**(4), 437–443 (2001).

13. N. Morishige, W. M. Petroll, T. Nishida, M. C. Kenney, and J. V. Jester, "Noninvasive corneal stromal collagen imaging using two-photon-generated second-harmonic signals," J. Cataract Refract. Surg. **32**(11), 1784–1791 (2006).
14. A. T. Yeh, N. Nassif, A. Zoumi, and B. J. Tromberg, "Selective corneal imaging using combined second-harmonic generation and two-photon excited fluorescence," Opt. Lett. **27**(23), 2082–2084 (2002).
15. H.-Y. Tan, Y. Sun, W. Lo, S.-J. Lin, C.-H. Hsiao, Y.-F. Chen, S. C.-M. Huang, W.-C. Lin, S.-H. Jee, H.-S. Yu, and C.-Y. Dong, "Multiphoton fluorescence and second harmonic generation imaging of the structural alterations in keratoconus ex vivo," Invest. Ophthalmol. Vis. Sci. **47**(12), 5251–5259 (2006).
16. T. Møller-Pedersen, H. D. Cavanagh, W. M. Petroll, and J. V. Jester, "Stromal wound healing explains refractive instability and haze development after photorefractive keratectomy: a 1-year confocal microscopic study," Ophthalmology **107**(7), 1235–1245 (2000).
17. H. Hennighausen, S. T. Feldman, J. F. Bille, and A. D. McCulloch, "Anterior-posterior strain variation in normally hydrated and swollen rabbit cornea," Invest. Ophthalmol. Vis. Sci. **39**(2), 253–262 (1998).
18. J. A. Izatt, M. R. Hee, G. M. Owen, E. A. Swanson, and J. G. Fujimoto, "Optical coherence microscopy in scattering media," Opt. Lett. **19**(8), 590–592 (1994).
19. A. L. Clark, A. Gillenwater, R. Alizadeh-Naderi, A. K. El-Naggar, and R. Richards-Kortum, "Detection and diagnosis of oral neoplasia with an optical coherence microscope," J. Biomed. Opt. **9**(6), 1271–1280 (2004).
20. S. Hodson, C. Wigham, L. Williams, K. R. Mayes, and M. V. Graham, "Observation on the human cornea in vitro," Exp. Eye Res. **32**(3), 353–360 (1981).
21. A. M. Larson and A. T. Yeh, "Ex vivo characterization of sub-10-fs pulses," Opt. Lett. **31**(11), 1681–1683 (2006).
22. A. Labbé, H. Liang, C. Martin, F. Brignole-Baudouin, J.-M. Warnet, and C. Baudouin, "Comparative anatomy of laboratory animal corneas with a new-generation high-resolution in vivo confocal microscope," Curr. Eye Res. **31**(6), 501–509 (2006).
23. B. R. Masters and M. Böhnke, "Three-dimensional confocal microscopy of the human cornea in vivo," Ophthalmic Res. **33**(3), 125–135 (2001).
24. W. M. Petroll, H. D. Cavanagh, and J. V. Jester, "Three-dimensional imaging of corneal cells using in vivo confocal microscopy," J. Microsc. **170**(Pt 3), 213–219 (1993).
25. D. W. Piston, B. R. Masters, and W. W. Webb, "Three-dimensionally resolved NAD(P)H cellular metabolic redox imaging of the in situ cornea with two-photon excitation laser scanning microscopy," J. Microsc. **178**(Pt 1), 20–27 (1995).
26. H. F. Li, W. M. Petroll, T. Møller-Pedersen, J. K. Maurer, H. D. Cavanagh, and J. V. Jester, "Epithelial and corneal thickness measurements by in vivo confocal microscopy through focusing (CMTF)," Curr. Eye Res. **16**(3), 214–221 (1997).
27. S. Pang, A. T. Yeh, C. Wang, and K. E. Meissner, "Beyond the 1/Tp limit: two-photon-excited fluorescence using pulses as short as sub-10-fs," J. Biomed. Opt. **14**(5), 054041 (2009).
28. J. V. Jester, T. Moller-Pedersen, J. Huang, C. M. Sax, W. T. Kays, H. D. Cavangh, W. M. Petroll, and J. Piatigorsky, "The cellular basis of corneal transparency: evidence for 'corneal crystallins'," J. Cell Sci. **112**(Pt 5), 613–622 (1999).
29. W. Radner and R. Mallinger, "Interlacing of collagen lamellae in the midstroma of the human cornea," Cornea **21**(6), 598–601 (2002).
30. W. Radner, M. Zehetmayer, R. Aufreiter, and R. Mallinger, "Interlacing and cross-angle distribution of collagen lamellae in the human cornea," Cornea **17**(5), 537–543 (1998).
31. A. Pandolfi and G. A. Holzapfel, "Three-dimensional modeling and computational analysis of the human cornea considering distributed collagen fibril orientations," J. Biomech. Eng. **130**(6), 061006 (2008).
32. P. M. Pinsky, D. van der Heide, and D. Chernyak, "Computational modeling of mechanical anisotropy in the cornea and sclera," J. Cataract Refract. Surg. **31**(1), 136–145 (2005).

1. Introduction

Mechanical properties of the cornea play a central role to its multifaceted function of serving as both a physical barrier and the primary refractive element in the eye. Yet, our present understanding of its mechanical response and underlying microstructural basis is derived from disparate measurements of tissue biomechanics and ultrastructure performed under different conditions and sample preparations. Indeed, cornea biomechanics have been found to affect seemingly routine intraocular pressure (IOP) measurements which appear to correlate with central cornea thickness and curvature, though in a non-straightforward manner as to preclude a simple correction for applanation tonometry [1–4]. Also, sophisticated ablation algorithms used to predict corneal response to refractive surgeries remain largely empirical, underscoring the need for better understanding of—or, at least, the need for technologies that can characterize—cornea mechanical properties in situ [5].

Traditionally, tissue mechanical properties are characterized by testing measurements that track the displacement of fiducial markers with applied loads [6–8]. For intact cornea, the placement of exogenous markers is limited to the epithelial or endothelial surface. However, the stroma comprises more than 90% of the cornea thickness and preferred orientations of the collagen lamellae in the superior-inferior and nasal-temporal directions in the central and circumferential orientation in the limbal regions suggest anisotropic mechanical responses [6,9]. Furthermore, there is accumulating evidence that the stroma is mechanically heterogeneous including ultrastructural measurements that showed more isotropic distribution of collagen lamellae in the anterior third compared with the posterior two-thirds [10], measurements of central cornea collagen microstructural responses to changes in IOP that exhibited differences among the anterior, mid, and posterior regions [11], and swelling experiments that attributed the maintenance of corneal curvature to a comparatively stiff anterior one-third relative to the posterior two-thirds [12].

Herein, we report the development of an integrated nonlinear optical and Fourier domain optical coherence microscopy system (NLOM-OCM) based on a Kerr-lens mode-locked sub-10-femtosecond titanium:sapphire laser and its application to the measure of both the mechanical and microstructural responses of the central cornea. With NLOM, endogenous nonlinear optical signals from cells (two-photon excited fluorescence from pyridine nucleotides and flavoproteins) and collagen (second harmonic generation, SHG) have been used to image cornea anatomy in normal [13,14] and diseased states [15] and to characterize collagen microstructural responses to changes in IOP [11]. Back reflection of incident laser light, primarily from corneal epithelia, endothelia, and keratocytes, has been used in elegant experiments with confocal microscopy that showed activated keratocytes following photorefractive keratectomy was the origin of corneal haze [16]. Furthermore, confocal reflectance microscopy has been used to measure anterior and posterior (endothelial) mechanical responses with a similar experimental design as reported here [17]. OCM is a closely related technique that uses low coherence interferometry in addition to a confocal pinhole to filter back scattered light [18]. OCM has an advantage in imaging depth [19], although both OCM and confocal reflectance microscopy generate images of tissue reflectance. As such, the NLOM-OCM system is shown to be sensitive to cornea anatomical structures and hydration state without using exogenous markers or labels. In addition, NLOM-OCM is used to characterize central cornea mechanical and collagen microstructural responses, as a function of depth layer-by-layer. Keratocyte nuclei are used as endogenous fiducial markers to measure mechanical responses and SHG in collagen is used to characterize stromal microstructural responses.

2. Methods

2.1. Cornea preparation

Corneas from New Zealand white rabbits (male; ~13 weeks; weight, 2-3 kg) were used and visibly transparent before, during, and after NLOM-OCM measurement. All experiments were performed on corneas less than 15 hours postmortem. Isolated corneas with a scleral rim were mounted on an artificial anterior chamber (K20-2125, ketene Products, Denville, NJ) for pressure control and imaging. Corneas were clamped at the sclera, imparting artificial boundary conditions. However, the clamping geometry of the chamber minimized stress on the sclera [20], and measured changes in thickness and microstructural morphology with pressure were repeatable and reversible.

The artificial anterior chamber provided a stable platform for cornea microscopy and intraocular pressurization. The base of the chamber had 2 ports fitted with silicone tubing, in-line pinch clamps, and female luer-lok connectors. One port was connected to a syringe filled with phosphate buffered saline (with 4% Dextran 70 to prevent cornea swelling) to control hydrostatic pressure. A manometer was connected in series on the second port for accurate

pressure readings. A rubber o-ring was placed on the chamber surrounding the mounted cornea to facilitate water coupling with the microscope objective in upright configuration. Before each imaging experiment, corneas were preconditioned through a pressure cycle (5–30 mm Hg) 3 times.

For swelling experiments, phosphate buffered saline without dextran was used in both the syringe-anterior chamber and water column (for the objective). NLOM-OCM images were acquired every 10-12 minutes over the course of one hour. Representative images are shown from a series with time stamp indicating delay from first image (Figs. 3A-D). Co-registered NLOM-OCM images (Figs. 3E-G) were acquired after an hour when morphology of keratocyte network appeared fully developed. Hydration state of corneas was monitored during experiments by keratocyte morphology and determined normal when only nuclei were apparent.
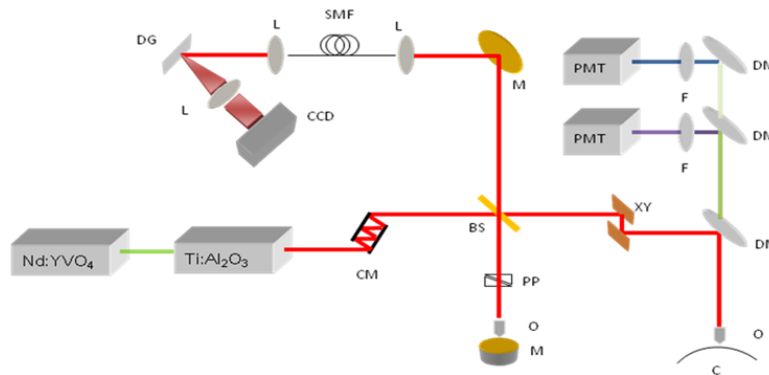
2.2. NLOM-OCM setup

Fig. 1. NLOM-OCM setup. BS, beam splitter; CM, chirp mirror; C, cornea sample; CCD, line scan camera; DG, diffraction grating; DM, dichroic mirror; F, filter; L, lens; M, mirror; O, objective; PMT, photomultiplier tube; SMF, single-mode fiber; XY, 2-axis scanning mirrors

Fourier domain OCM was integrated into an existing custom-built NLOM setup previously described [21]. A schematic of the integrated NLOM-OCM setup is shown in Fig. 1. Sub-10-fs laser pulses (800 nm, FWHM, 133 nm) from a Kerr-lens mode-locked $Ti:Al_2O_3$ oscillator (Femtosource compact, Femtolasers, Vienna, Austria) pumped by a frequency-doubled $Nd:YVO_4$ solid-state laser (Verdi, Coherent, Santa Clara, CA) were used as a common source for both NLOM and OCM. After the appropriate number of bounces from a pair of dispersion compensation mirrors (GSM 210, Femtolasers), the beam was split by a 50/50 beam splitter. One beam was directed to the cornea for NLOM and as the sample arm of OCM; the other was used as the reference arm of OCM. The beam in the sample arm was coupled into the epifluorescence port of an upright microscope (Axioskop2 MAT, Carl Zeiss, Thornwood, NY) and directed to the microscope objective ($40\times$ Achroplan, 0.8 NA or $63\times$ Achroplan, 0.95 NA, Carl Zeiss) by using a short-pass dichroic mirror (635dcspxruv3p, Chroma, Rockingham, VT). NLOM signals generated from the cornea were collected by the focusing objective and directed to a two-channel detector for image rendering at two different wavelengths for SHG (HQ405/40M, Chroma) and two-photon excited fluorescence (HQ525/50M, Chroma). Backscattered laser light from the sample was also collected by the focusing objective, reflected back to the beam splitter, and combined with the return beam from the reference arm. The combined beam was focused into a single mode fiber and directed to a home-built spectrometer. The beam coming out of the fiber was collimated, dispersed by a diffraction grating (NT43-211, Edmund Optics, Barrington, NJ), and focused with a custom objective onto a 2048-pixel line scan camera (L104k-2k, Basler, Exton, PA). Each pixel in the OCM image was generated by integrating the interferometric signal over the

source coherence length at the optical pathlength corresponding to the focal plane. Custom software written on the LabVIEW (National Instruments, Austin, TX) platform acquired NLOM and OCM images simultaneously with frame rate of 0.125 Hz. Two-dimensional (2D) en face images (256 X 256 pixels) were rendered by raster scanning the laser beam with a pair of galvanometer mirrors and image stacks of the cornea stroma were acquired with 1 μm increments at each pressure. Each image stack was acquired in two hours.

2.3. Strain calculation

Central cornea strain was calculated from OCM full thickness image stacks from seven corneas at five different IOPs (5, 8, 10, 15, 20 mmHg). The cornea was aligned for repeated measure of the same corneal features at all five pressures. The coordinates of centroids for three cell nuclei were identified in all five IOPs at each depth. To find nuclei centroids, a rectangular region around each cell nucleus was selected and a mean filter of 5 X 5 pixel sliding window applied. A threshold was used to determine the boundary, and the geometric center was calculated based on this boundary. Strain was calculated by nuclei displacement (geometric center) from their coordinates imaged at 5 mmHg (reference state). Using the coordinates of three nuclei in both the reference at 5 mmHg ($\Delta\mathbf{X}$) and deformed state ($\Delta\mathbf{x}$), the deformation gradient $\mathbf{F}$ was calculated by $\Delta\mathbf{x} = \mathbf{F} \cdot \Delta\mathbf{X}$. Green's strain $\mathbf{E}$ was calculated using $\mathbf{E} = \frac{1}{2}\left(\mathbf{F}^T\mathbf{F} - \mathbf{I}\right)$, where $\mathbf{F}^T$ is the transpose of $\mathbf{F}$ and $\mathbf{I}$ is the identity matrix. To compare the strains at different depths, the corneal stroma was subdivided into 10 equal thickness layers and the norms, $\|\mathbf{E}\| = \sqrt{trace(\mathbf{E} \cdot \mathbf{E}^T)}$, calculated in each layer were averaged.

2.4. NLOM (SHG) image processing

Image processing used with full thickness cross-sectional reconstructions of rabbit central cornea to better reveal the collagen lamellae architecture has been described previously [11]. Briefly, each 16-bit NLOM image was normalized (to 255), converted to 8-bit, Tagged Image File Format and input to MetaVue (V6.2r4, Universal Imaging Corp., Downingtown, PA) and AutoVisualize (v93, AutoQuant Imaging, Inc., Silver Spring, MD) for 3D reconstruction. For cross-sectional views shown in Fig. 6 below, nonlinear background subtraction was applied to adjust for non-uniform signal intensity through the central cornea cross-section. This operation applied a 10 X 10 pixel sliding window within which the minimum intensity value was subtracted from the first pixel. The window operated on every pixel of cross-sectional image incrementally; for operations within 10 pixels of image edge, the window was filled with values mirror-reflected across the image boundary. The original cross-sectional images are also shown for reference; see Fig. 6.

2.5. Statistical analysis

In both the strain and structural (interlamellar gap area) depth distribution data, the full thickness of the corneal stroma was divided into ten layers. As noted previously, collagen specific imaging by SHG revealed morphological features throughout the stroma that were characterized by an absence of signal (collagen) or interlamellar gaps (dark regions in Fig. 2C, bottom) [11]. Changes in interlamellar gap area in response to changes in IOP were attributed to microstructural responses. To statistically determine which layers of tissue have similar properties, MATLAB software (The Mathworks, Natick, MA) was used to perform a k-means clustering analysis on the strain and structural depth distribution at five pressures. In this clustering analysis, data are partitioned into k clusters with the nearest mean. The number of clusters, k, was determined by the correlative plot in Fig. 5 below.
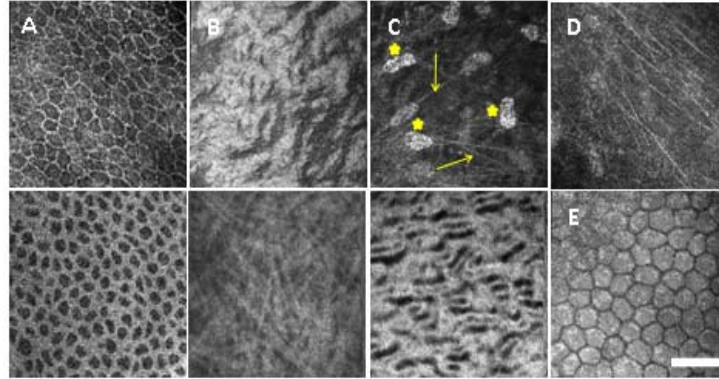
Fig. 2. Representative NLOM (lower) OCM (upper) images of rabbit cornea at different depths. Epithelium (A), epithelial-stromal boundary (B), stroma (C), Descemet's membrane by OCM (D) and endothelium (E). Stars and arrows indicate keratocyte nuclei and nerve fibers, respectively. Scale bar is 40 µm.

3. Results

3.1. Cornea anatomy

Complementary endogenous contrast mechanisms of integrated NLOM-OCM enable the imaging of rabbit cornea anatomy without exogenous stains or dyes. Representative NLOM-OCM images are shown in Fig. 2 of the different layers of rabbit cornea. Both backreflected light [22–24] and two-photon excited fluorescence [25] may be used in OCM and NLOM, respectively, to image the cobblestone morphology of the epithelium (Fig. 2A). However, because of their different contrast mechanisms, OCM and NLOM show complementary cell features. OCM signal is derived from backscattered light making it sensitive to changes in refractive index. Highlighted in OCM images of the epithelium were cell membrane and some nuclei (Fig. 2A, top). In contrast, two-photon excited fluorescence from factors related to the cell metabolic cycle (pyridine nucleotides and flavoproteins) was localized to the cytoplasm leaving dark nuclei and cell membranes (Fig. 2A, bottom) [14,25].

NLOM-OCM images from the underlying matrix of the epithelium are shown in Fig. 2B. The morphology of the basal lamina imaged by OCM (Fig. 2B, top) was consistent with that shown by confocal reflectance microscopy [26]. Weak SHG signal was detected from the collagen fibrils using NLOM (Fig. 2B, bottom) in contrast to the collagen lamellae of the stroma. In the stroma, keratocyte nuclei (stars) and nerve fibers (arrows) were visualized by OCM (Fig. 2C, top), and collagen lamellae were imaged using SHG by NLOM (Fig. 2C, bottom). The intrinsic signals from keratocyte nuclei (backscattered light) and collagen (SHG) were used in this study to characterize the central cornea mechanical response and underlying microstructure as a function of depth. Between the stroma and endothelium, Descemet's Membrane was marked by an absence of SHG signal (data not shown) and the presence of fibrous structures as observed by OCM (see Fig. 2D). The endothelium was revealed with OCM in Fig. 2E by high contrast between bright cell bodies and dark cell membranes.

3.2. Cornea swelling

Confocal reflectance microscopy has been used previously to reveal different keratocyte morphologies for corneas in the swollen state versus normal hydration [17]. Whereas keratocyte nuclei were prominent in normally hydrated corneas, nuclei and extended processes were revealed in swollen corneas and attributed to some combination of changes in keratocyte hydration and in refractive index of the surrounding matrix. Similar observations of keratocyte morphology were made with OCM depending on cornea hydration state. Nuclei of stromal keratocytes were observed with OCM in normally hydrated corneas whereas the

whole cell body with extended processes became visible with corneal swelling. This dynamic is shown for a single keratocyte in Fig. 3 as a function of swelling time. In Fig. 3A, the cornea was normally hydrated and only the keratocyte nucleus was visible. The intact cornea was exposed to phosphate buffered saline and swelled with time. As the cornea swelled, extended processes of the keratocyte became visible as shown in Figs. 3B–D. This effect of swelling on keratocyte morphology was used as real-time indicator of corneal hydration during NLOM-OCM measurements.
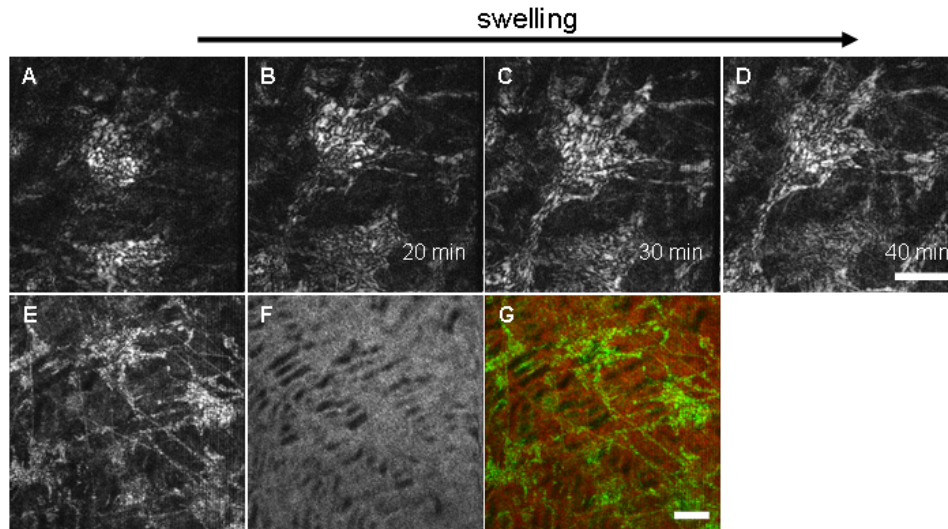

Fig. 3. Keratocyte morphology changes with corneal swelling. OCM images of same keratocyte at different hydration states shown in minutes past the first image (A-D). Co-registered NLOM-OCM images (E-G). False color was applied to OCM (green, E) and SHG (red, F) images and overlaid (G) to reveal the interrelationship between keratocyte network and underlying collagen matrix. The clear morphological changes provided verification of hydration state throughout the biomechanical imaging experiments. Scale bars are 20 µm.

An advantage of the integrated NLOM-OCM system is that the keratocyte network of swollen corneas can be imaged in the context of stromal collagen lamellae and segmented as shown in Figs. 3E–G. The keratocyte network of a swollen cornea imaged by OCM is shown in Fig. 3E. An NLOM image of the collagen matrix, shown in Fig. 3F, from the same field-of-view was acquired simultaneously using SHG. Green and red false colors were applied to the OCM and NLOM images, respectively, and overlaid in Fig. 3G to reveal the interrelationship between the keratocyte network and underlying collagen matrix.

3.3. Mechanical response depth profile

In our approach to characterizing the biomechanics of the central cornea, mechanical testing of the cornea was implemented by measuring the in-plane displacement of keratocyte nuclei as a function of IOP. OCM was used to measure nuclei displacement layer-by-layer through the full thickness of the stroma. Our methodology is illustrated in Fig. 4 for a given layer from within the central region of a rabbit cornea. Three keratocyte nuclei were tracked within a field of view at five pressures, 5 (Fig. 4A), 8 (Fig. 4B), 10 (Fig. 4C), 15 (Fig. 4D), and 20 mmHg (Fig. 4E). Coordinates of the keratocyte centroids were found from boundaries defined for the nuclei and used to calculate displacement at each pressure relative to the reference pressure of 5 mmHg. Where possible, sampling was increased by the tracking of multiple nuclei (up to five) and calculating in-plane displacements among sets of three. Full thickness image stacks acquired with 1 µm increments were subdivided into 10 layers by depth; calculated displacements were averaged for each layer.
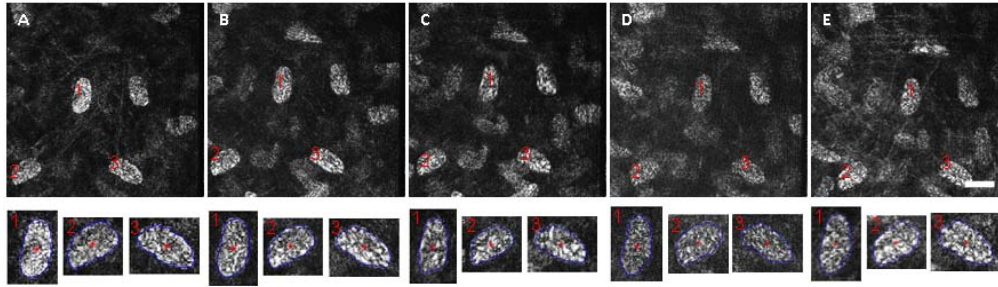
Fig. 4. Cell nuclei centroid identification and displacement calculation with changes in IOP from 5 mmHg (A) to 8 (B), 10 (C), 15 (D) and 20 mmHg (E). Scale bar is 20 μm.

The norm of in-plane (Green's) strain with IOP was calculated from the measured displacements and plotted as a function of depth in Fig. 5A. Ten mechanical response curves are shown, each corresponding to one of the 10 subdivided layers of the full thickness and numbered sequentially from the anterior. The results showed that the strain at each pressure increased with depth and that the mechanical response curves were nonlinear. Error bars are standard deviations calculated from averaging measurements from seven corneas. The first layer exhibited strains from 0.0176 to 0.0296 with standard deviations from 0.0014 (10 mmHg) to 0.0019 (15 mmHg) compared with the tenth layer which exhibited strains from 0.0415 to 0.0690 with standard deviations from 0.0008 (7 mmHg) to 0.0035 (20 mmHg). Rather than a continuous increase in strain, large changes in strain were observed from the sixth to seventh layer (and less so from the third to fourth layer). The sixth and seventh layers exhibited strains from 0.0290 to 0.0504 and from 0.0314 to 0.0617 with standard deviations from 0.0023 (10 mmHg) to 0.0037 (20 mmHg) and from 0.0022 (15 mmHg) to 0.0032 (20 mmHg), respectively. The third and fourth layers exhibited strains from 0.0212 to 0.0422 and from 0.0255 to 0.0455 with standard deviations from 0.0016 (20 mmHg) to 0.0024 (15 mmHg) and from 0.0014 (20 mmHg) to 0.0024 (15 mmHg), respectively.

To compare mechanical and collagen microstructural responses, a correlative plot between strain and interlamellar gap area is shown in Fig. 5B. Interlamellar gap area was calculated from collagen specific NLOM using SHG. These interlamellar gaps are characterized by an absence of SHG signal (see Fig. 2C, bottom and [11]). Each curve in the correlative plot corresponds to one of the 10 subdivided layers numbered from the anterior as in Fig. 5A. The data appear to cluster into three groups as the anterior (40%), mid (20%) and posterior (40%).
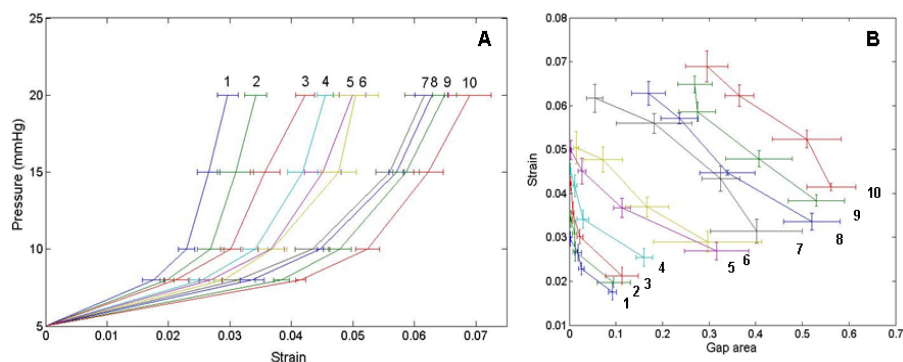

Fig. 5. Cornea strains (A) and its correlation with structural (gap area) responses (B) layer-by-layer. The pressure-strain curves combined with collagen microstructural responses can readily be grouped by depth as anterior (40%), transitional mid (20%) and posterior (40%) which is consistent with marked differences in mechanical responses between groups.

It should be noted that the mechanical (n = 5) and collagen microstructural responses (n = 7) were measured on different sets of corneas. Based on results of the correlative plot, three groups were assumed in a k-means clustering analysis of the mechanical and collagen microstructural responses data. The strain and structural depth distribution can be grouped into anterior, mid and posterior layers as (20:40:40) and (40:30:30), respectively.

Cross-sectional views of collagen lamellae through the full thickness of swollen (A,B) and normally hydrated corneal stroma (C-F) are shown in Fig. 6 at 5 (A-D) and 20 mmHg (E,F). Nonlinear background subtraction was implemented on the original images shown in Figs. 6A, C and E (see Section 2, Methods) to better reveal the collagen architecture in Figs. 6B, D and F. For reference, anterior and posterior 40% are demarked by dotted lines in normally hydrated cornea at 5 mmHg, see Figs. 6C, D, that divide the full thickness into three regions. Characteristic of views from swollen and normally hydrated hypotensive corneas (5 mmHg) are anterior lamellae interweave and transverse collagen segments aligned along the anterior-posterior axis (Figs. 6A–D). The length of these collagen segments is depth dependent with short (≤5 μm) anterior and long, regularly spaced posterior segments (as long as 50 μm in swollen corneas). Cross-sectional views of the same hypotensive cornea in Figs. 6C, D are shown at 20 mmHg in Figs. 6E, F and reveal thinning of the stroma with predominantly planar oriented collagen lamellae, though lamellae interweave and transverse segments were still evident anteriorly and posteriorly, respectively.
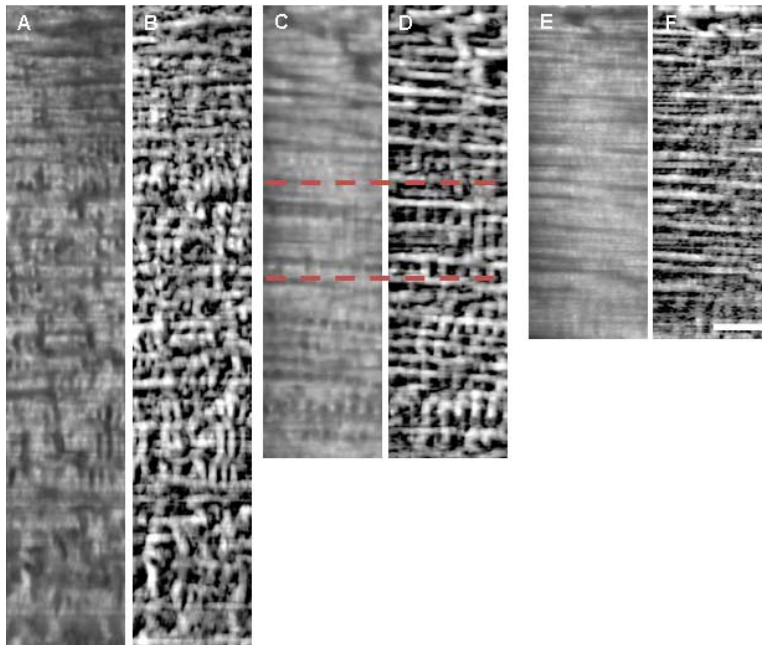

Fig. 6. Cross-sectional collagen structure of swollen (A,B) and normally hydrated cornea (C-F) at 5 mmHg (A and C, raw; B and D, processed) and 20 mmHg (E, raw; F, processed). Scale bar is 40 μm.

4. Discussion

An integrated NLOM-OCM system was developed utilizing a sub-10-fs Kerr-lens mode-locked Ti:Al$_2$O$_3$ laser as a common source. These pulses are an order of magnitude shorter in duration than what is typically used in NLOM systems that results in an order of magnitude improvement in peak power (for a given pulse energy) with which to generate nonlinear optical signals for image rendering. For two-photon processes such as SHG, the improvement

in signal generation scales as the inverse pulse duration; for two-photon excited fluorescence, signal generally follows this same relationship but will ultimately depend on the overlap between the pulse two-photon excitation and molecular (two-photon) absorption spectra [27].

The use of sub-10-fs pulses ensures co-registration of the NLOM and OCM images. Whereas lateral resolution of the modalities is limited by diffraction, axial resolution of OCM is determined to a first approximation by the coherence length of light. Thus, in integrating NLOM and OCM with a common source, its coherence length, which is inversely proportional to bandwidth, should compare with the confocal parameter of the focusing objective. For the $40 \times$, 0.8 NA objective used in our measurements, the confocal parameter is ~1.9 µm (Rayleigh approximation) which is comparable with the 2.12 µm coherence length of the laser.

NLOM-OCM provides comprehensive microstructural information of cornea without the use of exogenous stains or dyes. Major components of the rabbit cornea were imaged including cells (epithelial, keratocytic, and endothelial), nerves and extracellular matrix, especially the collagen lamellae. This anatomical information can be used to characterize physiological state of the cornea. For example, keratocyte morphology was used as an experimental indicator of cornea hydration state. OCM visualization of keratocyte nuclei was shown to expand to include the cell body and processes with corneal swelling. Under normal hydration, keratocyte nuclei were highly scattering compared with the cell body. Light scattering may be mitigated in the cell body by balance of refractive indices between the cell cytoplasm and extracellular environment. Within the cell body, the refractive index may be regulated by crystallin proteins [28]. Upon swelling, the balance in refractive index between the extracellular environment and crystallin regulated cytoplasm may be disrupted resulting in the heightened OCM signal from keratocyte cell body and extended processes. Our data suggest, though it were not quantified, that swelling results in changes in intra- and extracellular refractive indices as observed in the OCM image of keratocyte network and faint extracellular matrix in Fig. 3E.

In this study, the developed NLOM-OCM system was used to measure depth-dependent mechanical responses of rabbit central cornea. A traditional mechanical testing approach was used where (in-plane) displacement among fiducial markers was measured as a function of applied force, in this case IOP. Keratocyte nuclei were used as endogenous markers [17] that enabled layer-by-layer characterization in situ without destruction of tissue. It should be noted that only keratocyte nuclei displacement were measured in this study which limited biomechanical characterization to the stroma between the basal lamina and Descement's membrane. Based on the contrast observed from NLOM-OCM images of the epithelium and endothelium, extending these mechanical testing measurements to those layers, as done previously with exogenous markers [6–8], should be straight forward.

Depth dependent mechanical response curves were nonlinear and exhibited distinct behavior in three regions, anterior, transitional mid and posterior, see Fig. 5A. Typically, a cell nucleus has an area of about 800 pixels and the coordinates of nuclei centroids were repeatable to within one-tenth of a pixel (0.57 µm by 0.57 µm). The displacements were measured between nuclei separated by tens of micrometers. Thus, more than 60 pixels separated centroids in typical measurements with displacements of about three pixels. Indeed, these results were consistent with previous mechanical tests that showed larger posterior than anterior strains [6,17]. In particular, strains presented here were similar to those measured with comparable methodology, i.e., measure of nuclei displacement as a function of IOP by confocal reflectance microscopy [17]. However, there are a few notable differences between the studies. Here, Green's strain norms, $\|\mathbf{E}\|$, and its depth dependence were reported based on calculations from keratocyte displacements layer-by-layer through the stroma. In the previous work, average principal strain was reported and displacements were measured among keratocytes from an anterior layer and among the endothelium. Also, results presented here

were measured on isolated cornea with scleral rim mounted on an artificial anterior chamber versus whole globe with 20-gauge needle inserted into the anterior chamber. Whereas thickness changes for swollen and normally hydrated corneas of the whole globe were less than 10% from hypo- to hypertensive IOP [17], thickness changes in this study were as large as 30% in swollen and 25% in normally hydrated corneas from 5 to 20 mmHg. Boundary conditions imposed by the artificial anterior chamber and undetected corneal swelling (based on keratocyte morphology) may have contributed to this discrepancy as well as structural alterations from cornea isolation.

The marked differences in mechanical responses exhibited by the anterior, mid, and posterior central cornea correlate with microstructural organization and responses of the collagen lamellae. Small strains of the anterior correspond with interlaced lamellae and short (≤5 μm) transverse collagen segments that were best viewed at low tension, particularly in swollen corneas (see Figs. 6B, D). Mid stroma was characterized as a transitional region with longer, more regularly spaced transverse collagen segments. In contrast to collagen organization of the anterior were regularly organized, long transverse segments of the posterior stroma. In swollen corneas, these transverse segments in the posterior measured as long as 50 μm (see Fig. 6B and [11]).

The observation of transverse collagen lamellae in hypotensive corneas was in stark contrast to layered lamellae in normo-/hypertensive cornea, see Fig. 6. Changes in thickness with IOP suggested swelling as well as other hydration effects. Cross sectional thickness of swollen lamellae may increase in size giving the appearance of transverse segments, though this may not completely explain its depth dependent lengths, as long as 50 μm in the posterior stroma. Previous studies have reported interlaced collagen lamellae in human cornea using electron microscopy [29,30]. In those experiments, cornea preparation for electron microscopy included NaOH treatment for ground substance removal and physically stretching the tissue along the anterior-posterior axis. Hydration effects in this study may have achieved this same mechanical effect, exposing interlaced lamellae, albeit with minimal disruption to the native tissue.

The measured mechanical response depth profile correlates with our previous measurements of collagen lamellae responses to the changes in IOP (see Fig. 5B). Characteristic of stromal collagen morphology particularly at low tension were interlamellar collagen-free spaces or gaps. As a fraction of the NLOM image area, these gaps decreased with increased IOP in a depth dependent manner. Anterior gaps were characterized by an immediate decrease in fractional area in contrast with posterior gaps which persisted even at hypertensive IOP [11]. Between the mechanical response study here and the previous collagen microstructural response study, there was a slight mismatch in the statistical groupings of the layers by k-means clustering. Otherwise, the correlation between the two studies was remarkable given the limited number of samples (12 corneas).

Current biomechanical models of the cornea employ finite element methods because of the tissue's complicated geometry and have incorporated nonlinear response and predominant collagen fiber orientations [31,32]. By incorporating nonlinear response and predominant fiber orientations, characteristic soft tissue and anisotropic responses along the meridian can be described. However, a limitation in these models is an assumption of tissue homogeneity, not necessarily resulting from the mathematical formulations directly, but rather due to the lack of regional mechanical data, particularly as a function of depth. Our methodology, when applied to corneas within the whole globe, enables further investigation of cornea biomechanics without assuming tissue homogeneity a priori.

In summary, we report the direct measurement of cornea mechanical responses in the central stromal region using NLOM-OCM. The methodology used in this study may be expanded to comprehensively map regional mechanical responses throughout the cornea ex vivo. These experimental measures will further understanding of tissue mechanical properties by providing essential validating data to mathematical models of cornea mechanics.

Acknowledgments